



Flow distribution and maximum current density studies in redox flow batteries with a single passage of the serpentine flow channel



Xinyou Ke ^{a, b}, J. Iwan D. Alexander ^{a, c, d}, Joseph M. Pahl ^a, Robert F. Savinell ^{b, c, *}

^a Fluid Mechanics Lab, Department of Mechanical and Aerospace Engineering, Case Western Reserve University, Cleveland, OH 44106, United States

^b Electrochemical Engineering and Energy Lab, Department of Chemical Engineering, Case Western Reserve University, Cleveland, OH 44106, United States

^c Great Lakes Energy Institute, Case Western Reserve University, Cleveland, OH 44106, United States

^d School of Engineering, University of Alabama at Birmingham, Birmingham, AL 35294, United States

HIGHLIGHTS

- A mathematical model of a fuel cell-like flow battery has been developed.
- The model predicts a small flow penetration into a carbon paper electrode.
- Reactant penetrating an electrode limits the current density of the flow battery.
- Predicted maximum current densities match published experimental results.

ARTICLE INFO

Article history:

Received 7 May 2014

Received in revised form

22 July 2014

Accepted 23 July 2014

Available online 1 August 2014

Keywords:

Mass transport

Convection

Limiting current density

Zero-gap flow battery model

Vanadium flow battery

ABSTRACT

Flow batteries show promise for very large-scale stationary energy storage such as needed for the grid and renewable energy implementation. In recent years, researchers and developers of redox flow batteries (RFBs) have found that electrode and flow field designs of PEM fuel cell (PEMFC) technology can increase the power density and consequently push down the cost of flow battery stacks. In this paper we present a macroscopic model of a typical PEMFC-like RFB electrode-flow field design. The model is a layered system comprised of a single passage of a serpentine flow channel and a parallel underlying porous electrode (or porous layer). The effects of the inlet volumetric flow rate, permeability of the porous layer, thickness of the porous layer and thickness of the flow channel on the flow penetration into the porous layer are investigated. The maximum current density corresponding to stoichiometry is estimated to be 377 mA cm^{-2} and 724 mA cm^{-2} , which compares favorably with experiments of $\sim 400 \text{ mA cm}^{-2}$ and $\sim 750 \text{ mA cm}^{-2}$, for a single layer and three layers of the carbon fiber paper, respectively.

© 2014 Elsevier B.V. All rights reserved.

1. Introduction

Redox flow batteries have gained unprecedented attention for energy storage applications. Well-suited for and scalable to utility scale storages, they can be employed to cope with intermittent power generation from renewable energy sources, such as solar and wind energy and are a useful tool for load leveling, peak shaving and emergency back up to improve the stability of the power grid [1,2]. Several research groups are currently

working on redox flow batteries. Skyllas-Kazacos et al. [3,4] developed an all-vanadium redox flow battery (all-VRFB) that was motivated by earlier studies on iron–chrome as a redox couple [5]. An advantage of the all-VRFB is that species crossover leads to only a temporary capacity loss in contrast to a permanent capacity loss for the flow cells with two or more different elements acting as anions or cations in the electrolyte; examples being iron–chromium [6], bromine–polysulfide [7] and zinc–bromine [8], etc. Most recent studies are focused on vanadium flow cells, especially for the all-VRFB. Savinell et al. [9] developed an all-iron flow cell with a potential advantage of very low costs. Chiang et al. [10] invented a semi-solid lithium rechargeable flow battery within using active slurry porous electrode material through reaction chambers and an improved current density is achieved. Aziz et al. [11] has introduced an organic & inorganic

* Corresponding author. Electrochemical Engineering and Energy Lab, Department of Chemical Engineering, Case Western Reserve University, Cleveland, OH 44106, United States. Tel.: +1 216 368 272; fax: +1 216 368 3016.

E-mail address: rfs2@case.edu (R.F. Savinell).

RFB with quinone reactants in an aqueous electrolyte. High current density and discharge capacity retention have been demonstrated.

Computational modeling approaches have been reported to explore performance improvements in RFB flow cells [12–18]. Walsh et al. developed several mathematical flow battery models [14–17] that describe isothermal [14], non-isothermal [15], hydrogen [16] and oxygen evolution [17] (with bubble formation) transport processes in electrochemical reactions. These models include diffusion, convection and migration. A dilute-solution approximation method was incorporated. Vynnycky [18] proposed an asymptotic model for a large-scale cell stack to save computational time while improving the calculation efficiency.

Few experimental and numerical studies on details of flow fields for RFBs have been reported. Kjeang et al. [19] designed a microfluidic vanadium redox flow cell with a high aspect ratio Y-shape micro flow channel over a porous carbon substrate to obtain a peak power density of 70 mW cm^{-2} , which is small for large-scale energy storage applications. Recently, Zawodzinski et al. [20–22] and Mench et al. [21,22] designed flow cell stack configurations for RFBs to improve current density and power density. These designs are based on modern cell designs employed in PEM fuel cells and allow operation at much higher current densities as compared to earlier conventional flow batteries. In these designs the electrolyte flows through serpentine channels behind a porous electrode. This is different

from the conventional flow battery designs where the electrolyte flows through a carbon felt electrode. Specifically, a polarization curve analysis method [20] was used to analyze performance losses in two types of flow cell configurations: (a) a simple battery (SB) with a carbon felt electrode embedded in the PVC compartments and (b) a modified fuel cell with a serpentine flow channel fuel cell battery (FCB) over the carbon felt (FCB-F) or the carbon fiber paper electrode (FCB-P). A higher limiting current density was obtained in the FCB-P than in the SB. A peak power density of 557 mW cm^{-2} , which is more than five times that obtained using conventional flow cell configurations, was achieved at 60% state of charge by adopting a “zero-gap” serpentine flow channel flow battery architecture [21]. A superior behavior for lower over-potential was observed in the flow cells composed of two negative porous electrode layers. The potential effects of thermally pretreated porous electrodes and ion selective membranes on the performance of the “zero-gap” serpentine flow cell were also investigated [22]. A peak power density of 767 mW cm^{-2} was obtained by using three layers of carbon fiber paper with an oxidative thermal pretreatment and the Nafion 212 membrane. It was pointed out that surface morphologies and oxygen concentrations might alter the surface functionalization.

Chen et al. [23] conducted experiments on a parallel flow structure together with CFD analysis for flow distributions in the all-VRFB, but generated a very low power density of 15.9 mW cm^{-2} . It appears that flow rates may be highly variable

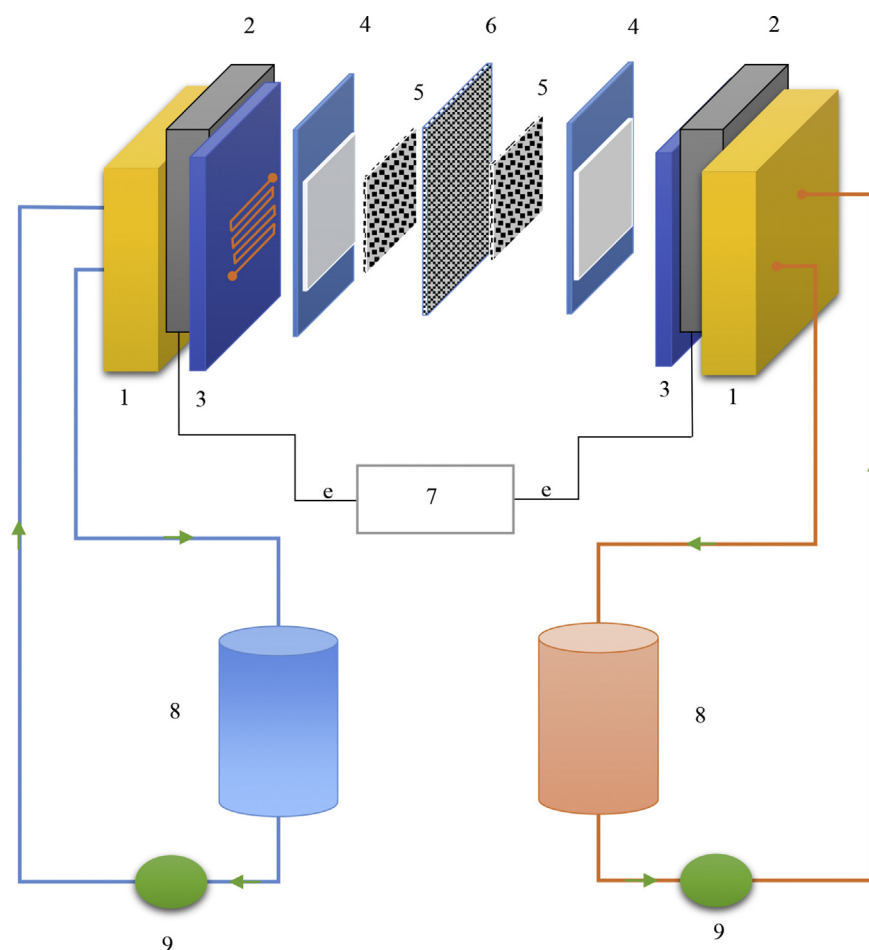


Fig. 1. The flow cell compartment: 1-end plates; 2-current collectors; 3-graphite plates with serpentine flow channels; 4-gaskets; 5-porous electrodes; 6-ion selective membrane; 7-load; 8-electrolyte tanks and 9-pumps.

over the cell, which has motivated calls for an optimized flow field. Xu et al. [24] made output performance comparisons among different VRFBs with no flow, serpentine and parallel flow channels. The VRFBs with the serpentine flow channels was found to have a higher round trip efficiency. Latha et al. [25] carried out experiments on a serpentine flow field of VRFBs. The effects of rib convection, porous electrode compression on flow distributions and pressure drops were studied. Several comprehensive reviews of RFBs can be found in the literature [26–29].

In this paper, a model is presented that helps explain the maximum current density based on rates of consumption of flow reactants that can be achieved with a single passage of the “zero-gap” serpentine flow channel flow battery design.

2. Flow cell configurations

A redox flow battery cell with serpentine flow channels is shown in Fig. 1 and this architecture is originally from the work of Zawodzinski and Mench et al. [21]. This construction consists of the following components: 1-end plates; 2-current collectors; 3-graphite plates with the serpentine flow channels; 4-gaskets; 5-porous electrodes; 6-ion selective membranes; 7-load; 8-electrolyte tanks and 9-pumps. The left and right sides of the flow cell compartment are anode and cathode, respectively. During the discharge process, the electrolytes in the tanks are circulated by the pump and pass through the serpentine flow channels over the surface of the porous electrodes and are accompanied by electrochemical reactions.

3. Macroscopic mathematical model

A mathematical model is developed to better understand the mass transport mechanism for electrolyte flowing through a single passage of the serpentine flow channel and over the

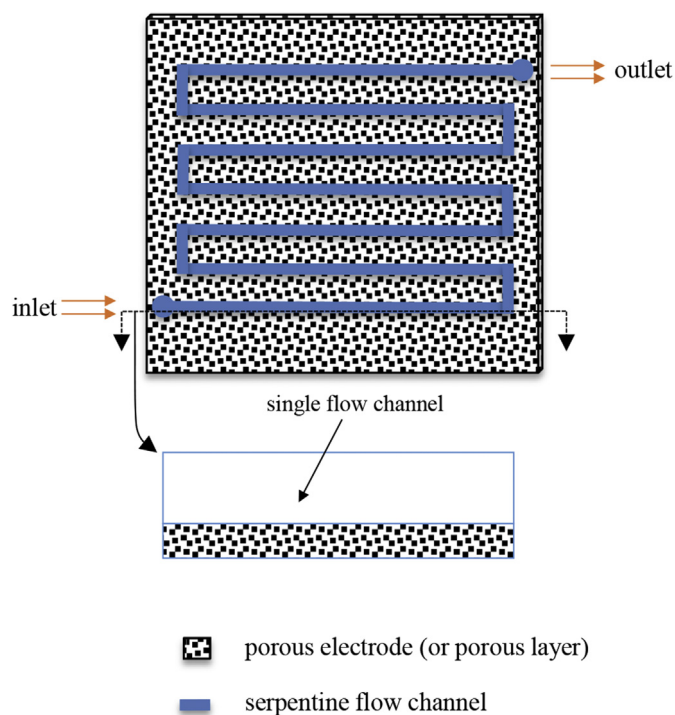


Fig. 2. Flow segment modeled of the serpentine flow channel with the porous electrode as shown in Fig. 1.

porous electrode. Particular attention is given to the investigation of the flow dynamics within the porous electrode. The transport theorem [30–32] and averaging volume method [33] are applied to establish the macroscopic model, which is largely based on previous studies of Whitaker [31–33], Gary et al. [34], Howes et al. [35], Ochoa-Tapia et al. [36,37], Goyeau et al. [38] and Bars et al. [39].

The flow passage segment modeled here is shown in Fig. 2. The current collector and ion selective membrane bounded by the porous electrode and the serpentine flow channel are not represented in Fig. 2. The flow pattern could be considered as a 2D (X, Y) simplification of a 3D (X, Y, Z) system. The 2D macroscopic model is shown in Fig. 3. It illustrates macroscopic physical structures for the porous electrode, including a representative “average” elements for the porous solids, adjoining electrolyte fluid, and the interface between electrolyte fluid and porous solids. Here, Ω_f and Ω_p denote the domain of the flow channel and the porous electrode, respectively. Σ_{cf} , Σ_{fp} and Σ_{pm} are the corresponding interfaces between the current collector and the flow channel, the flow channel and the porous electrode and the porous electrode and the ion selective membrane. For each representative element for the porous solids and their neighboring electrolyte fluid, γ and σ denote, respectively, liquid phase and solid phase and quantities represent a locally average value.

The source of the average dynamic motion in the porous layer is derived based on the assumptions of steady, incompressible, Newtonian and laminar flow.

$$0 = -\varepsilon_\gamma \nabla \cdot \langle P_\gamma \rangle^\gamma + \mu_\gamma \nabla^2 \mathbf{u}_\gamma - \mu_\gamma \varepsilon_\gamma k_{\gamma\sigma}^{-1} \langle \mathbf{u}_\gamma \rangle + \varepsilon_\gamma \rho_\gamma \mathbf{g} \quad (1)$$

Eq. (1) is the macroscopic mathematical model for the dynamic motion in the porous layer. If the second term (viscous force term) of the right side for Eq. (1) is neglected, then, it reduces to Darcy's law, which states that the superficial velocity is proportional to the permeability of the porous material and the gradient of the average pressure exerted on the flow but inversely proportional to the dynamic viscosity of fluid. It's easy to infer that Darcy's law deals with the flow pattern without regarding viscous force term (Brinkman term) [40]. However, the viscous force term is taken into consideration in this macroscopic mathematical model, which incorporates Darcy's law and Brinkman's term. Thus, Eq. (1) is named as Brinkman–Darcy model. Navier–Stokes motions are applied in the flow channel. The non-dimensional forms for the dynamic motions and boundary conditions are shown below. In later discussions, ε_γ , μ_γ , ρ_γ , $k_{\gamma\sigma}$, $\langle P_\gamma \rangle^\gamma$ and $\langle \mathbf{u}_\gamma \rangle$ will be replaced with ε , μ , ρ , k , $\langle P_p \rangle$, and $\langle \mathbf{u}_p \rangle$ or $\langle \mathbf{v}_p \rangle$.

3.1. Non-dimensionalization

Based on the assumptions mentioned above and neglect the effects from gravity, the normalized forms for fluid dynamic motions become corresponding Eqs. (2) and (3) in X and Y directions in the flow channel. Eqs. (4) and (5) are expressed for the dimensionless flow patterns in the porous layer in X and Y directions, respectively. Non-dimensional parameters are defined in Table 1.

$$\begin{aligned} & Re \frac{(t_f + t_p)^2}{t_f \cdot L} u_f^* \frac{\partial u_f^*}{\partial X^*} + Re \frac{(t_f + t_p)}{t_f} v_f^* \frac{\partial u_f^*}{\partial Y^*} \\ & = -Re \frac{(t_f + t_p)^2}{t_f \cdot L} \frac{\partial p_f^*}{\partial X^*} + \frac{(t_f + t_p)^2}{L^2} \frac{\partial^2 u_f^*}{\partial X^{*2}} + \frac{\partial^2 u_f^*}{\partial Y^{*2}} \end{aligned} \quad (2)$$

Table 3
Geometry, electrolyte properties and operation parameters.

Parameters	Value	Sources
Thickness of flow channel (t_f)	0.1 cm	Measured
Width of flow channel (w_f)	0.1 cm	Measured
Length of flow channel (L)	2 cm	Measured
Thickness of a single porous layer (t_p)	0.041 cm	[21]
Density of electrolyte (ρ)	1.354 g cm ⁻³	[55]
Dynamic viscosity of electrolyte (μ)	4.928×10^{-3} Pa s	
Working temperature (T)	298.15 K	
Initial ion concentration (c)	0.001 mol cm ⁻³	[21]
Inlet volumetric flow rate (Q_{in})	20 ml min ⁻¹ & 20 ml min ⁻¹ to 30 ml min ⁻¹	[12,21]

4. Pre-computational analysis

4.1. Physical parameters

Before employing a computational fluid dynamics (CFD) solver-COMSOL Multiphysics based on discretized domains, boundary conditions and related algorithms, 2D physical parameters are determined. Parameters for geometry, electrolyte properties and operating conditions are given in Table 3. The RFB flow cell with the serpentine flow channels is evolved from direct methanol fuel cell (DMFC) or proton exchange membrane fuel cell (PEMFC) laboratory cell hardware, and the thickness (or depth), width and length for a single passage of the serpentine flow channel are measured to be 0.1 cm, 0.1 cm and 2 cm, respectively. The thickness for a single layer of carbon fiber paper is ~0.041 cm [21]. The thickness of the porous layer is altered from 0.041 cm to 0.287 cm (the number of the porous layers ranges from 1 to 7) to investigate the effects of thickness of the porous layer on the mass flow transport from the flow channel into the porous layer. This model is considered as isothermal with an approximation as the working temperature of 298 K [54]. The density and dynamic viscosity of the electrolyte are given in Table 3. Walsh et al. [13–17], Qiu et al. [55] treated the bulk electrolyte as water while Knehr et al. [12] found the density and dynamic viscosity of negative and positive electrolyte were slightly different. The inlet volumetric flow rate $Q_{in} = 20$ ml min⁻¹ gives $u_{in} = 33.3$ cm s⁻¹ based on the dimensions of the cross section of the flow channel and Q_{in} is altered from 5 ml min⁻¹ ($u_{in} = 8.3$ cm s⁻¹) to 30 ml min⁻¹ ($u_{in} = 50$ cm s⁻¹) to study the inlet volumetric flow rates on the flow penetration into the porous layer. Table 4 gives the properties of the porous layer, including three kinds of foametal, carbon fiber paper and graphite felt porous materials. The foametal specimens were used for the experimental studies of Beavers and Joseph [41] to analyze the boundary conditions of the Poiseuille flow over a permeable interface. The carbon fiber paper [28] and the graphite felt [24] are typical porous materials for the porous electrodes used in the RFB flow cells.

Table 4
Properties of porous layer materials.

Porous layer samples	Pore (d_{po}) or fiber (d_f) diameter, [μ m]	Porosity ε	Permeability k , [m ²]	Estimated permeability k_{ck} , [m ²] ^a	Sources
Foametal A	406 (pore)	0.78	9.7×10^{-9}	9.0×10^{-9}	[38,40]
Foametal B	864 (pore)	0.78	3.94×10^{-8}	4.1×10^{-8}	
Foametal C	1140 (pore)	0.79	8.2×10^{-8}	8.1×10^{-8}	
Carbon fiber paper	10 (fiber)	0.8	2.0×10^{-11}	2.3×10^{-10}	[28]
Graphite felt	17.6 (fiber)	0.7	Not given	2.1×10^{-10}	[24]

^a Estimated by Eq. (4).

Pore diameters are given for the foametal A, foametal B and foametal C while fiber diameters are given for the carbon fiber paper and the graphite felt. Goyeau et al. [38] made estimations of the porosity for the foametals in Table 4, and the Kozeny-Carman model [56,57] shown as Eq. (6) is used to predict the permeability of the porous samples.

$$k = \frac{d^2 \varepsilon^3}{C_{kc}(1 - \varepsilon)^2} \quad (6)$$

where, d is the pore diameter or fiber diameter. The permeability is directly correlated with pore diameter or fiber diameter while inversely correlated with the Kozeny-Carman constant. Carman pointed out that experimental C_{kc} was around 180 for the pore diameter. Walsh et al. [13–17] and Qiu et al. [55] considered C_{kc} as 5.55 for the fiber diameter, then the estimated permeability of the carbon fiber paper ($d_f = 10$ μ m, $\varepsilon = 0.8$) is around 2.3×10^{-10} m² and this is consistent with Tomadakis et al. [58] who thought the permeability was $\sim 1 \times 10^{-10}$ m² as a 3D random fiber model was built for the carbon fiber paper with 10 μ m fiber diameter and 0.8 porosity. However, Weber et al. [28] considered permeability as 2×10^{-11} m² for the carbon fiber paper reported in Table 4. In this study, the value of 2.3×10^{-10} m² is employed for the estimated permeability for the carbon fiber paper with 10 μ m fiber diameter and 0.8 porosity. The permeability of the graphite felt is predicted from Eq. (6) as 2.1×10^{-10} m². The relationship between

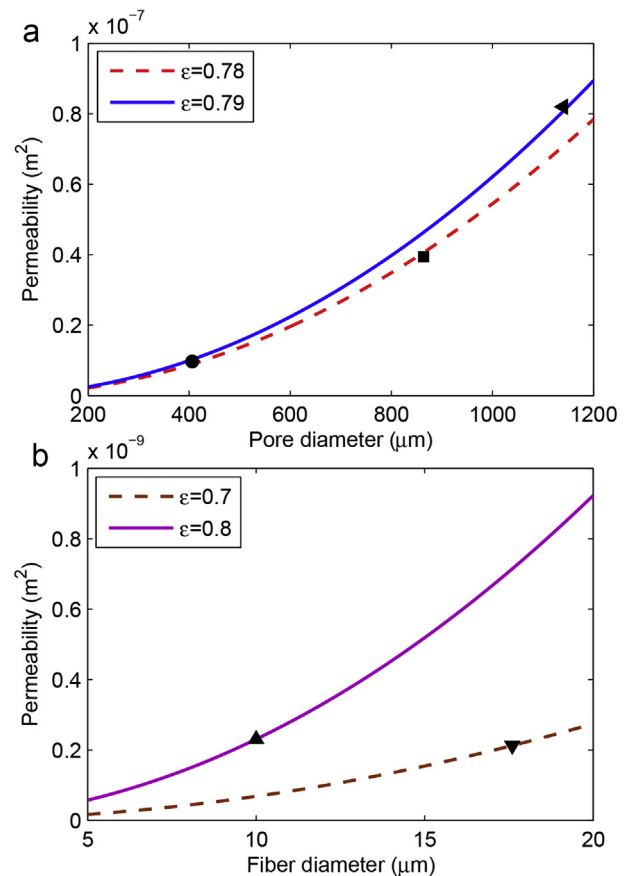


Fig. 4. The relationship between pore diameter or fiber diameter and permeability under specific porosities mentioned in Table 4 is curved through using the Kozeny-Carman model: (a) the foametal: ●- $\varepsilon = 0.78$, $k = 9.7 \times 10^{-9}$ m²; ■- $\varepsilon = 0.78$, $k = 3.94 \times 10^{-8}$ m²; ◀- $\varepsilon = 0.79$, $k = 8.2 \times 10^{-8}$ m² and (b) the carbon fiber paper: ▲- $\varepsilon = 0.8$, $k = 2.3 \times 10^{-10}$ m²; the graphite felt: ▼- $\varepsilon = 0.7$, $k = 2.1 \times 10^{-10}$ m².

permeability and pore diameter or fiber diameter under a specific porosity is shown in Fig. 4, the permeability is predicted through the Kozeny-Carman model with considering $C_{kc} = 180$ for the pore diameter and $C_{kc} = 5.55$ for the fiber diameter.

Pore and fiber diameters have a great effect on the permeability. Increasing the pore diameter from 100 μm to 1000 μm or fiber diameter from 10 μm to 20 μm , the permeability is elevated by a factor of 100 and 4 for the pore diameter and fiber diameter, respectively. Active surface area (a_s) of porous fibers can be estimated by the filament analog model developed by Carta et al. [59] within building the porous fibers as cylinder models as shown in Eq. (7)

$$a_s = \frac{4(1 - \varepsilon)}{d_{fi}} \quad (7)$$

The variations of the active surface area with fiber diameters are shown in Fig. 5 for the carbon fiber paper and the graphite felt. The fiber diameter strongly affects the active surface area. Increasing the fiber diameter from 5 μm to 15 μm , the active surface area is decreased by a factor of 3. However, the porous fibers in reality are not perfect cylinders, and the complex shapes of the porous solids are beyond our discussions. The tradeoff between the permeability and the active surface area needs further study.

The values for the inlet volumetric flow rates, inlet velocities and Reynolds numbers are given in Table 5. Because of the Reynolds number ranging from 22.8 to 137, the flow regime is considered as laminar flow.

5. Results and discussion

5.1. Normalized flow patterns

The flow hydrodynamics are dominated by Navier–Stokes motions in the flow channel Ω_f and Brinkman–Darcy model in the

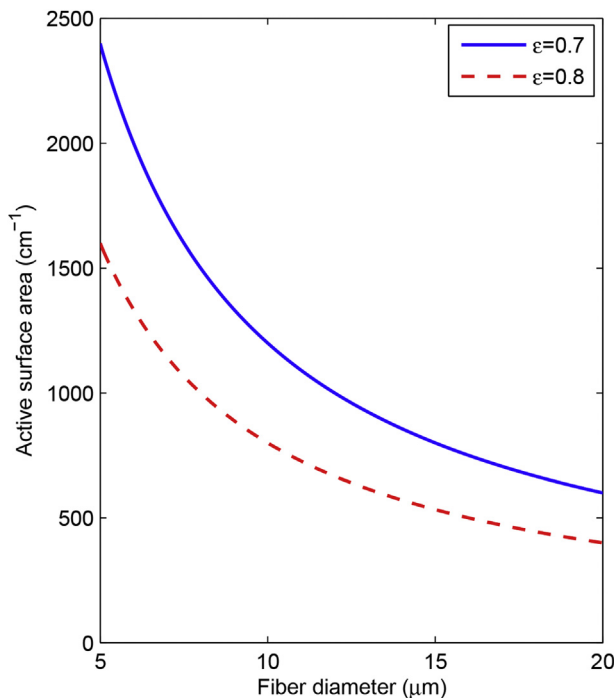


Fig. 5. The variations of active surface area (a_s) for the carbon fiber paper and the graphite felt as the fiber diameter increases from 1 μm to 20 μm by using the filament analog model [59] within building porous fibers as cylinder models.

Table 5

Value for Q_{in} , u_{in} and Re using geometry dimensions given in Table 3.

Q_{in} (ml min ⁻¹)	u_{in} (cm s ⁻¹)	Re
5	8.3	22.8
10	16.7	45.9
15	25	68.7
20	33.3	91.5
25	41.7	115
30	50	137

porous layer Ω_p . In order to clearly see the flow patterns, larger permeability ($9.7 \times 10^{-9} \text{ m}^2$) of the porous layer is chosen. The flow velocities in the X direction (u_f^* and $\langle u_p \rangle^*$) are illustrated below while the flow velocities in the Y direction (v_f^* and $\langle v_p \rangle^*$) are not shown because in most of the flow channel and the porous layer, the velocities v_f^* and $\langle v_p \rangle^*$ are much smaller compared with corresponding u_f^* and $\langle u_p \rangle^*$ except at the very beginning and end of the flow channel and the porous layer. Fig. 6 describes the trend of normalized u_f^* and $\langle u_p \rangle^*$ along X^* ranging 0 to 1 for six different Y^* under the ideal plug flow inlet condition as the Re (Reynolds number) is 91.5. In the Ω_f domain, u_f^* climbs from 1 to 1.4 as the flow regime changes from uniform to fully developed state. However, at near to the front edge of the Ω_p region, $\langle u_p \rangle^*$ sharply increases to a peak value, then decreases as the fully developed region is approached. The hydrodynamic entrance length L_e is calculated to be 0.46 cm as the centerline velocity is 99% of the fully developed centerline velocity. About 75% of the flow channel is fully developed. For the case of conventional pipes or circular ducts, the normalized entrance length L_e^* is ~6% of Reynolds number for the laminar flow. Atkinson et al. [60] and Chen et al. [61] proposed correlations (Eqs. (8) and (9)) between the non-dimensional hydrodynamic flow entrance length L_e^* and the Reynolds number for the laminar flow through the parallel plate flow channel.

$$L_e^* = C_1 + C_2 Re \quad (8)$$

$$L_e^* = \frac{C_3}{(C_4 Re + 1)} + C_5 Re \quad (9)$$

where, $L_e^* = L_e/t_f$, $C_1 = 0.625$, $C_2 = C_5 = 0.044$, $C_3 = 0.63$, $C_4 = 0.035$.

The corresponding estimated L_e are 0.465 cm and 0.418 cm from correlations (8) and (9). These entrance length predictions have a reasonable agreement with the numerically computed entrance length of 0.46 cm. Some back flow occurs in the porous layer with a small X^* as shown in Fig. 7. Using a smaller inlet volumetric flow rate ($Q_{in} = 5 \text{ ml min}^{-1}$) of 8.3 cm s^{-1} for u_{in} with 22.8 for Re , L_e is computed to be 0.134 cm. Thus, the extent of the fully developed region is over 93% of the flow channel (see Fig. 8). The estimated L_e from Eqs. (8) and (9) are seen to be reasonable with the numerical result of 0.134 cm at 0.163 cm and 0.135 cm, respectively. If Q_{in} is in the range of 20 ml min^{-1} to 30 ml min^{-1} (Knehr et al. [12]), then the corresponding values of L_e then lie in the range of 0.46 cm–0.67 cm. This illustrates that roughly 65%–75% of the flow channel is fully developed. In later sections, the volume flow rate of $Q_{in} = 20 \text{ ml min}^{-1}$ ($u_{in} = 33.3 \text{ cm s}^{-1}$) is used to analyze the maximum current density for the carbon fiber paper electrodes. It is emphasized that our model is not the same as a parallel flow plate channel. For latter, the BC#4 should be “no slip” instead of continuity of the velocity and the normal stress at the interface mentioned in Table 2. Thus, some accuracy is lost for the entrance length prediction when correlations (8) and (9) are used. From both Figs. 6 and 8, an over-shoot is found in the velocity profile of the

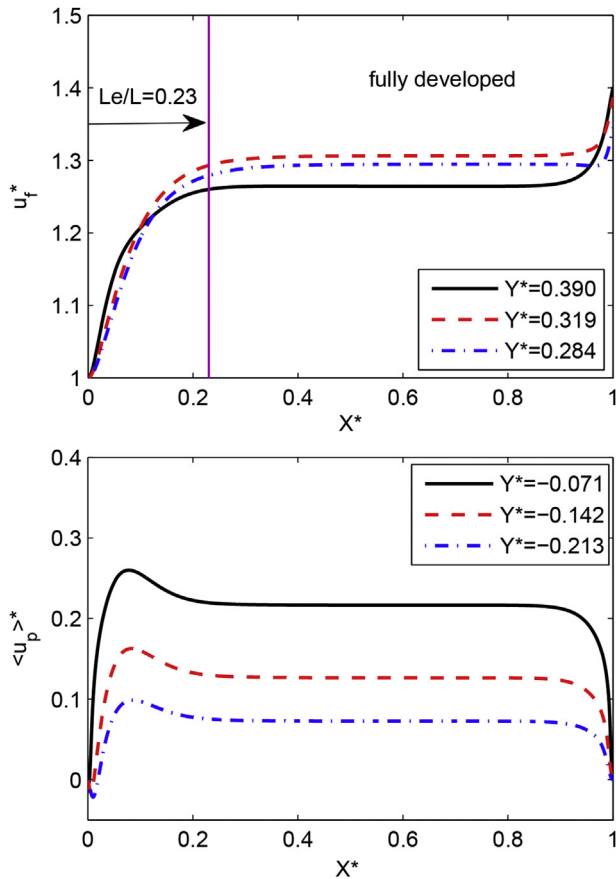


Fig. 6. The trend of normalized u_f^* and $\langle u_p \rangle^*$ with X^* from 0 to 1 at six Y^* : 0.390, 0.319, 0.284, -0.071, -0.142 and -0.213 in the Ω_f and the Ω_p ($k = 9.7 \times 10^{-9} \text{ m}^2$, $\varepsilon = 0.78$, $Re = 91.5$, $t_f = 0.1 \text{ cm}$, $t_p = 0.041 \text{ cm}$).

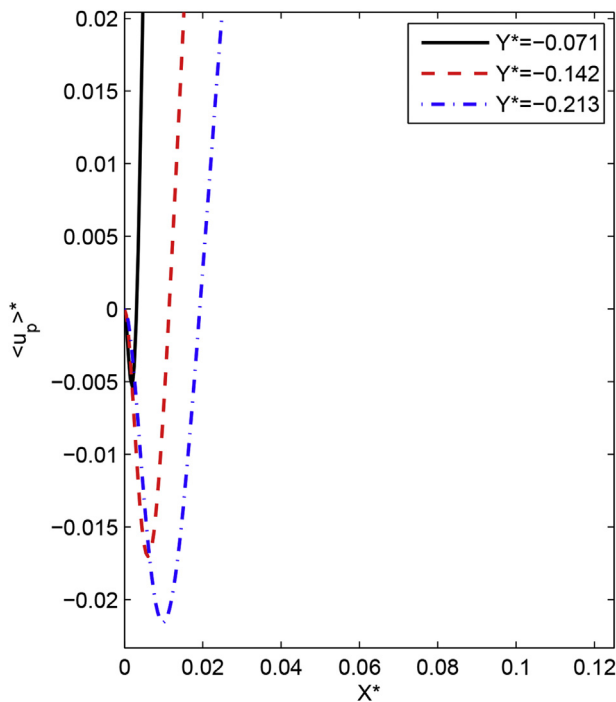


Fig. 7. The enlarged local curves of Fig. 6(a).

porous layer with a small X^* . This is expected, and is caused by the assumption of the ideal plug flow at the entrance interface providing momentum to drive the fluid into the porous layer near to the left wall (BC#5). However, this over-shoot disappears when the ideal parabolic flow inlet condition is adopted as mentioned in the work of Ke [62]. Fig. 9 describes the trend of normalized u_f^* and $\langle u_p \rangle^*$ along Y^* from -0.291 to 0.709 for four specific X^* : 0, 0.1, 0.2 and 0.7 representing the entrance through the developing, developed and fully developed regions. It is seen that the normalized average velocity $u_{f,avg}^*$ decreases from 1 to 0.921, then increases to 0.934 while $\langle u_p \rangle_{avg}^*$ exhibits an opposite trend and climbs from 0 to 0.179, then decreases to 0.150 as the fully developed region is approached. The normalized averages $u_{f,avg}^*$ and $\langle u_p \rangle_{avg}^*$ for Y^* with X^* are described by Eqs. (10) and (11), respectively.

$$\left(u_{f,avg}^*\right)_{X^*} = \frac{t_f + t_p}{t_f} \int_0^{\frac{t_f}{t_f+t_p}} u_f^*(X^*, Y^*) dY^* \quad (10)$$

$$\left(\langle u_p \rangle_{avg}^*\right)_{X^*} = \frac{t_f + t_p}{t_p} \int_{-\frac{t_p}{t_f+t_p}}^0 \langle u_p \rangle^*(X^*, Y^*) dY^* \quad (11)$$

Eqs. (10) and (11) give the average dimensionless velocity in a specific X^* along Y^* .

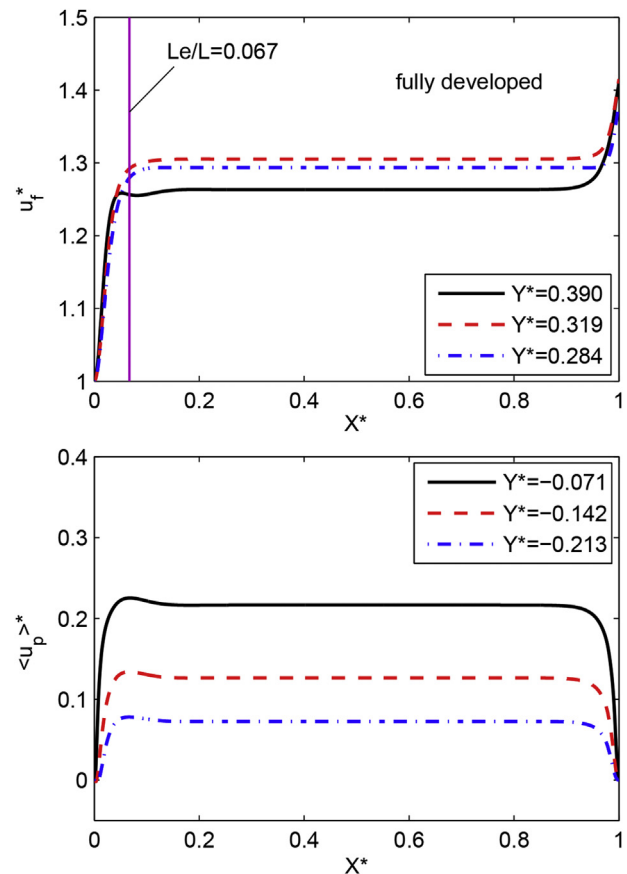


Fig. 8. The trend of normalized u_f^* and $\langle u_p \rangle^*$ with X^* from 0 to 1 at six Y^* : 0.390, 0.319, 0.284, -0.071, -0.142 and -0.213 in the Ω_f and the Ω_p ($k = 9.7 \times 10^{-9} \text{ m}^2$, $\varepsilon = 0.78$, $Re = 22.8$, $t_f = 0.1 \text{ cm}$, $t_p = 0.041 \text{ cm}$).

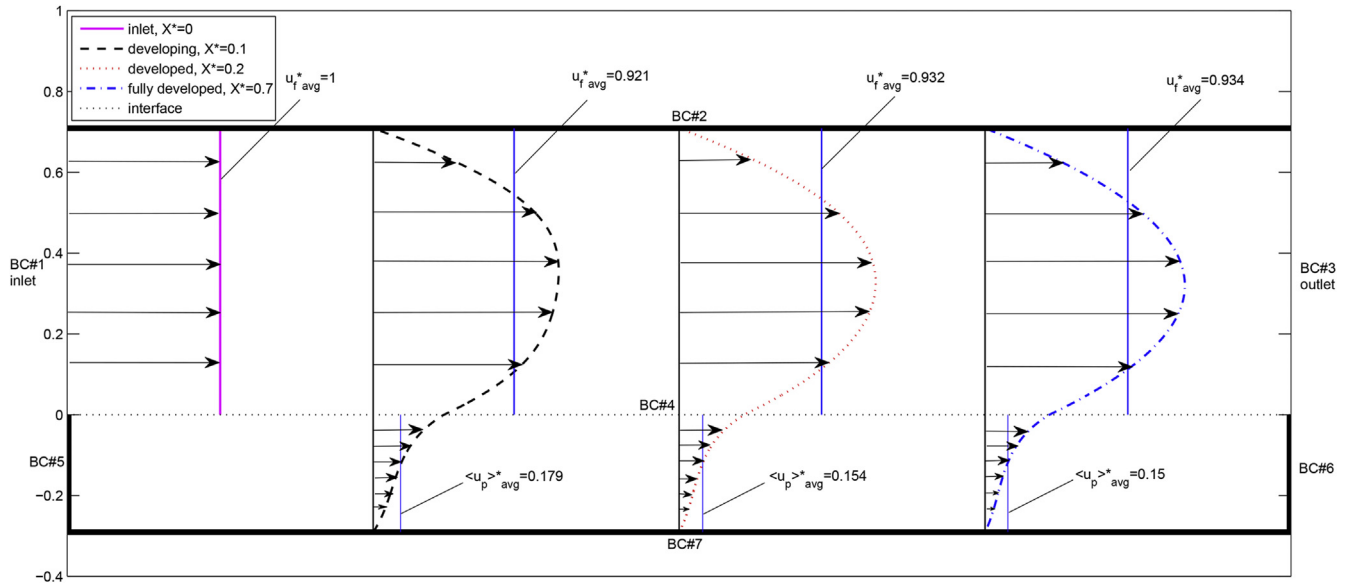


Fig. 9. Non-dimensionalization flow configurations for u_f^* and $\langle u_p \rangle^*$ with Y^* from entrance to developing, developed and fully developed region in the Q_f and the Q_p at four X^* : 0, 0.1, 0.2 and 0.7 ($k = 9.7 \times 10^{-9} \text{ m}^2$, $\varepsilon = 0.78$, $Re = 91.5$).

5.2. Inlet volumetric flow rate & permeability effects

The effects from inlet volumetric flow rates on flow distributions for the fully developed region are shown in Fig. 10. The flow penetration into the porous layer increases as the inlet flow rate

climbs from 10 ml min^{-1} to 30 ml min^{-1} . Fig. 11 illustrates the effects of the permeability on the enhancement of flow penetration into the porous layer. This clearly shows that the permeability has a more dominant influence than the inlet volumetric flow rate on the increase of flow penetration into the porous layer.

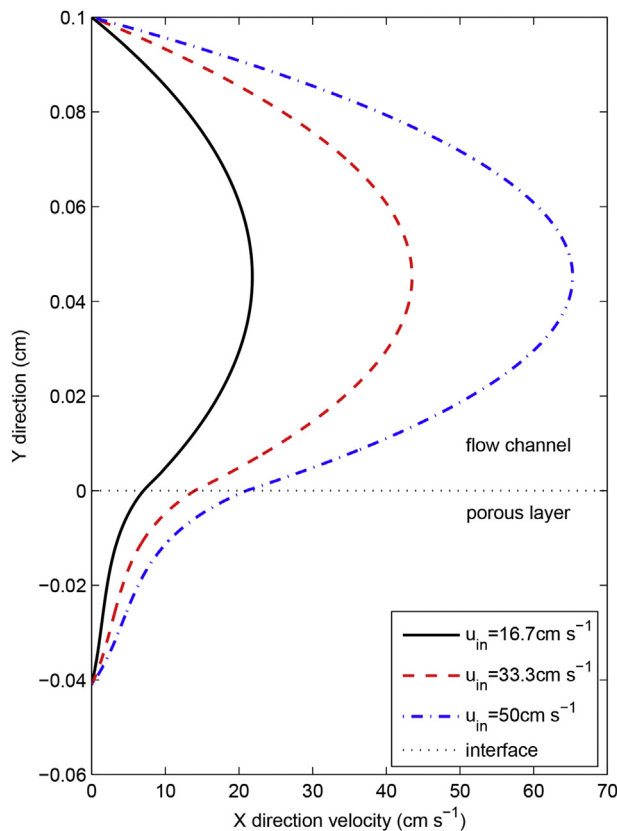


Fig. 10. u_f and $\langle u_p \rangle$ profiles along the Y direction for the fully developed region: inlet volumetric flow rate Q_{in} climbs from 10 ml min^{-1} to 30 ml min^{-1} (u_{in} ranges from 16.7 cm s^{-1} to 50 cm s^{-1} , $k = 9.7 \times 10^{-9} \text{ m}^2$, $\varepsilon = 0.78$, $t_f = 0.1 \text{ cm}$, $t_p = 0.041 \text{ cm}$).

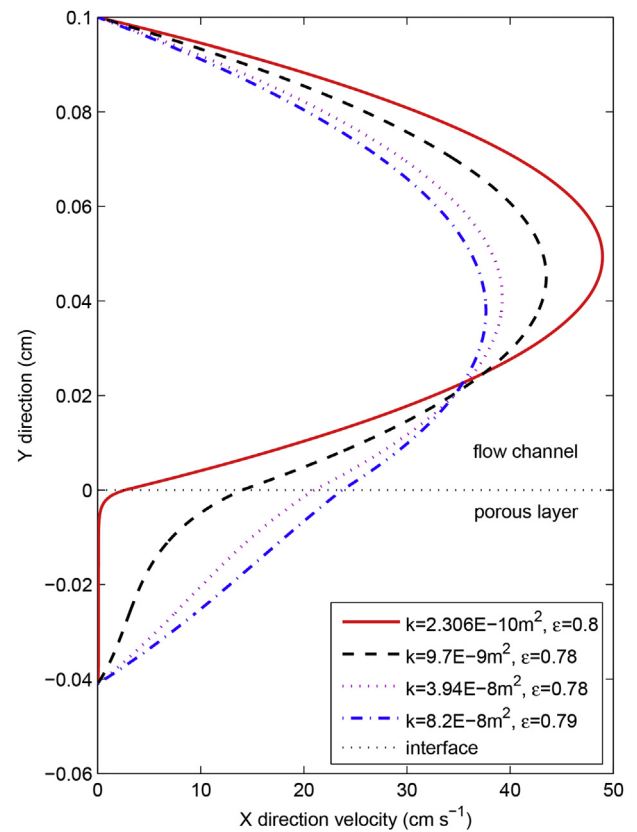


Fig. 11. u_f and $\langle u_p \rangle$ profiles along the Y direction for the fully developed region: permeability increases from $2.3 \times 10^{-10} \text{ m}^2$ to $8.2 \times 10^{-8} \text{ m}^2$ for the foametal and the carbon fiber paper porous material in Table 4 ($t_f = 0.1 \text{ cm}$, $t_p = 0.041 \text{ cm}$, $u_{in} = 33.3 \text{ cm s}^{-1}$).

5.3. Thickness of porous layer & flow channel effects

The effects of the thickness of the porous layer and the flow channel on flow distributions along the Y direction have been studied. Fig. 12 depicts the flow distributions for the fully developed region at three different thicknesses of the porous layer: 0.041 cm (single porous layer), 0.123 cm (three porous layers) and 0.205 cm (five porous layers) with the fixed 0.1 cm flow channel depth. More flow is transferred from the flow channel into the porous layer with a larger thickness of the porous layer. The influence of the depth of the flow channel is illustrated in Fig. 13 under the same inlet velocity condition. More flow goes into the porous layer with thinner flow channels even though this corresponds to a smaller inlet volumetric flow rate.

5.4. Volumetric flow rate in the porous layer

The flow penetration into the porous layer can be estimated by the following equation:

$$Q_p = w_p \int_{-t_p}^0 \langle u_p \rangle_{fd} dY \quad (12)$$

The relationship between Q_p and t_p under inlet volumetric flow rate Q_{in} ranging from 5 ml min⁻¹ to 30 ml min⁻¹ for the typical carbon fiber paper used in the RFB flow cells is shown in Fig. 14. The value of Q_p is a small fraction of the inlet volumetric flow rate. For example, for t_p of 0.123 cm (three porous layers), Q_p is estimated to be 3.74×10^{-4} cm³ s⁻¹ when Q_{in} is 5 ml min⁻¹.

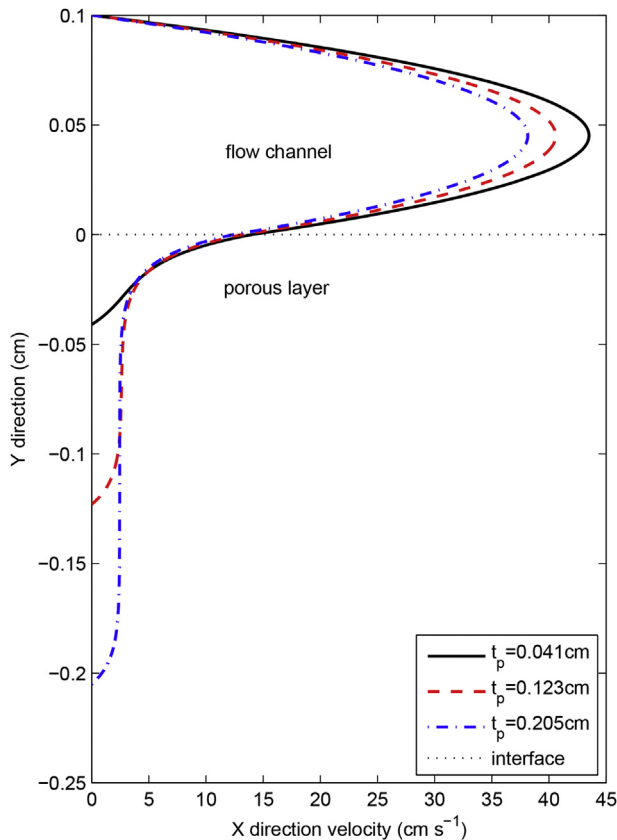


Fig. 12. u_f and $\langle u_p \rangle$ profiles along the Y direction for three different thicknesses of the porous layer: 0.041 cm (single porous layer), 0.123 cm (three porous layers) and 0.205 cm (five porous layers) for the fully developed region ($t_f = 0.1$ cm, $u_{in} = 33.3$ cm s⁻¹, $k = 9.7 \times 10^{-9}$ m², $\varepsilon = 0.78$).

5.5. Limiting and maximum current density

As electrolyte flows through the porous electrode, the electrochemical reactions at the electrolyte interface within the porous layer result in current flow, which is determined by the species flux to the solid surface, Faraday constant and the number of transferring electrons per mole of reactant consumed during the reaction. The species flux to the porous solid interface is related to diffusion, convection and migration processes. The current density is limited to the situation where the concentration of reactant at the solid electrode interface goes to zero. In this case, the concentration over-potential contributes a large efficiency loss. In order to minimize a concentration over-potential, the operating current density is usually chosen to be not larger than 25% of the limiting current density. The limiting current density (based on approximate membrane area) can be estimated from the Fick's law.

$$i_{lim} = \frac{at_p n F D c}{\delta} \quad (13)$$

where, n is the number of electrons transferred per mole of species reacted, F is Faraday constant, D is diffusivity, c is the bulk electrolyte concentration, t_p is the thickness of the porous electrode, ' a ' is the interfacial electrode area per unit of porous electrode volume, and δ is the thickness of diffusion layer. Eq. (13) also can be written as

$$i_{lim} = at_p n F k_m c \quad (14)$$

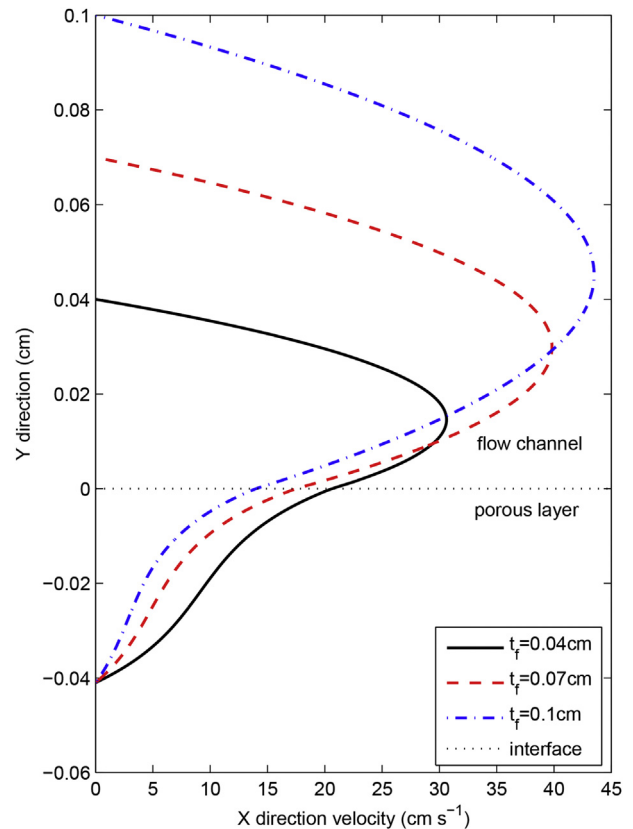


Fig. 13. u_f and $\langle u_p \rangle$ profiles along the Y direction for three different thicknesses of the flow channel: 0.04 cm, 0.07 cm and 0.1 cm for the fully developed region ($t_p = 0.041$ cm, $u_{in} = 33.3$ cm s⁻¹, $k = 9.7 \times 10^{-9}$ m², $\varepsilon = 0.78$).

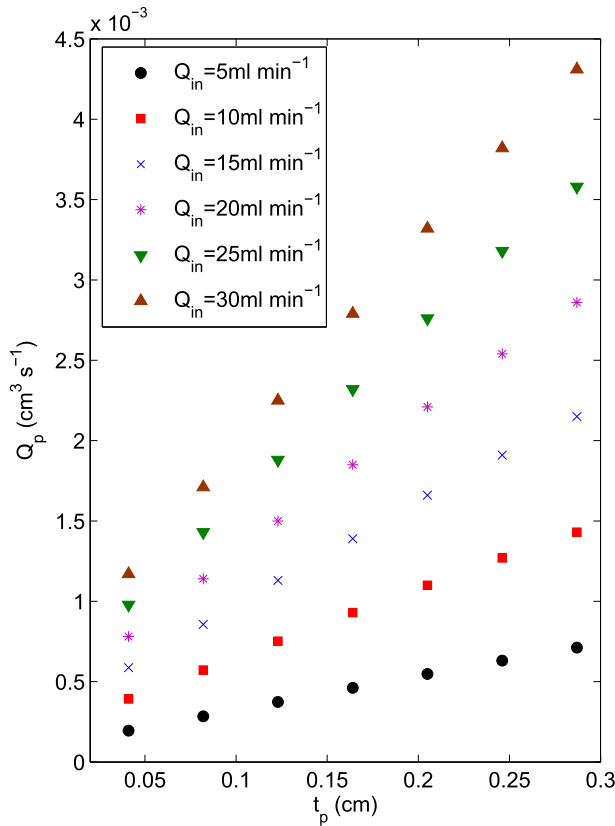


Fig. 14. The relationship between Q_p and t_p as Q_{in} ranging from 5 ml min⁻¹ to 30 ml min⁻¹ for the typical carbon fiber paper used in the RFB flow cells ($k = 2.3 \times 10^{-10}$ m²).

where, k_m represents the local mass transfer coefficient at the interface between the porous electrode solid phase and the bulk flowing electrolyte solution. Recently, Zawodzinski and Mench et al. [21] tested a flow battery with the serpentine flow channel modified from DMFC or PEMFC flow cell as shown in Fig. 15(b), (c), and (d). Compared with the conventional RFBs as shown in Fig. 15(a), this flow cell has a thin porous layer (typical ~0.04 cm)

and it can lead to a lower ohmic loss while enabling a higher limiting current density. In the limiting case of no electrolyte penetration into the porous electrode, the limiting current density can be estimated by Eq. (15) [63]

$$i_{lim} = 0.9783 \frac{nFDc}{L} \int_0^L \left(\frac{\langle u_f \rangle}{t_f DX} \right)^{\frac{1}{3}} dX \quad (15)$$

Using Eq. (15) and the following values for inlet volumetric flow rate ($Q_{in} = 20$ ml min⁻¹), the geometry for the single flow channel ($t_f = w_f = 0.1$ cm, $L = 2$ cm), bulk concentration ($c = 0.001$ mol cm⁻³), diffusivity ($D = 10^{-6}$ cm² s⁻¹) and assuming no electrolyte penetration, the limiting current density is estimated to be about 78 mA cm⁻². However, this predicted value significantly underestimates the reported maximum current density ~400 mA cm⁻² and ~750 mA cm⁻² observed for a single layer and three layers of the carbon fiber paper in Refs. [21], respectively. One can conclude from these estimates that convection in the porous layer is important to support such large current densities. An estimate of the maximum current density can be made by assuming the reaction is limited by the total flow reactant consumption in the porous layer, or the stoichiometric consumption, and ohmic losses are assumed to be neglected. Applying a mass balance and Faraday's law gives

$$i_{max} = \frac{nFcQ_p}{w_p L} \quad (16)$$

where, Q_p is obtained in previous sections of this paper and as shown in Fig. 14 and w_p is equal to w_f . In this estimate, we assume a very large interfacial mass transfer coefficient in Eq. (14). The estimation of maximum current density for a number of layers for the carbon fiber paper is given in Fig. 16. It can be seen that as the number of the porous layer increases from 1 to 3, the maximum current density increases from 377 mA cm⁻² to 724 mA cm⁻². Results for one layer and three layers of the carbon fiber paper compare favorably to the experimental results of Zawodzinski and Mench et al. [21] as shown in Fig. 16. The inlet volumetric flow rate ($Q_{in} = 20$ ml min⁻¹) in the flow channel causes flow in the porous electrode Q_p of 7.81×10^{-4} cm³ s⁻¹ (single porous layer, $t_p = 0.041$ cm) and 1.50×10^{-3} cm³ s⁻¹ (three porous layers,

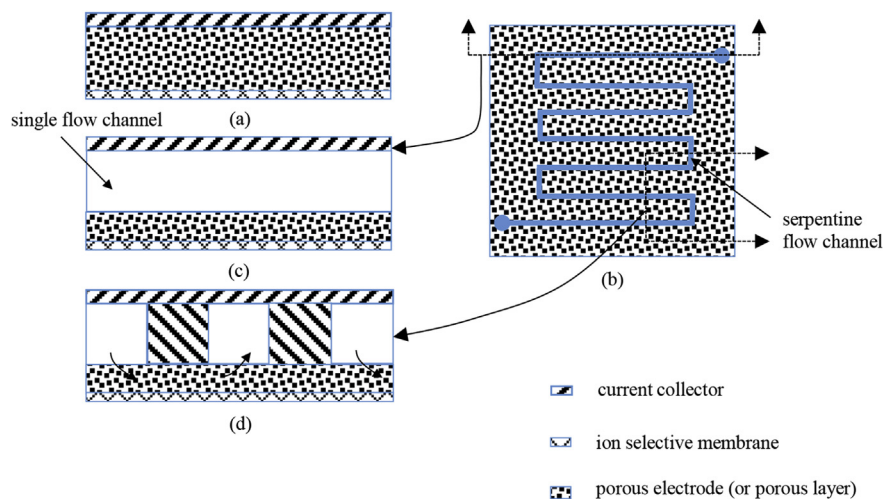


Fig. 15. (a) A thick porous electrode for the conventional RFBs; (b) a RFB flow cell with the serpentine flow channel modified from DMFC or PEMFC; (c) a single passage of the serpentine flow channel with a thin porous layer, cross section view of (b); (d) adjoint flow channels with a thin porous layer, cross section view of (b).

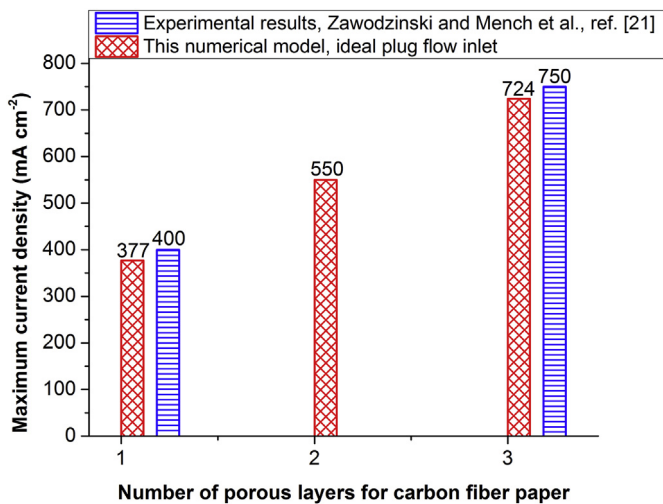


Fig. 16. The relationship between the maximum current density possible from the flow reactant supply and the number of porous layers for the carbon fiber paper ($Q_{in} = 20 \text{ ml min}^{-1}$, $c = 0.001 \text{ mol cm}^{-3}$, $L = 2 \text{ cm}$, $k = 2.3 \times 10^{-10} \text{ m}^2$).

$t_p = 0.123 \text{ cm}$) from Fig. 16, then the maximum current density is estimated to be 377 mA cm^{-2} and 724 mA cm^{-2} , respectively.

The estimates of maximum current density above are based on the assumptions for electrolyte properties, cell design parameters and estimated permeability of the porous electrode. The estimated maximum current density is very dependent on the permeability of the porous layer. These calculations use a permeability of $2.3 \times 10^{-10} \text{ m}^2$, which may be large according to Weber et al. [28] ($2 \times 10^{-11} \text{ m}^2$). Using a smaller permeability predicts a much smaller amount of flow penetrating into the porous layer, and thus a lower maximum current density. The pressure drop along one flow channel and then along the adjacent returning flow channel will create a pressure gradient driving force that drives fluid into the adjacent flow channel through the porous layer. In this case, the distance between the adjacent flow channels are short (see Fig. 15(d)), and this by-pass of electrolyte through the porous electrode will supply reactant to the electrode similar to our model, except modified by a factor of about 10 (flow channel length divided by the average distance between the two adjacent flow channels). Consequently, the estimate of the maximum current density due to the bypass flow again gives a reasonable estimate of the maximum current density as compared to experimentally reported value for the lower estimate of permeability of $2 \times 10^{-11} \text{ m}^2$.

Our model as shown in Eq. (16) is based on the contact area between the flow channel and the porous electrode, and this area is smaller than the membrane area. But, the actual penetration of flow into the porous layer is likely under-estimated since flow through the porous layer can extend beyond the width of the channel. Furthermore, the interdigitated flow channels as mentioned by Aziz et al. [11] would direct all flow through the porous layer, and consequently a higher maximum current density could be achieved.

6. Conclusions

A 2D macroscopic mathematical model is established to capture the dynamic flow patterns in RFBs represented by a single passage of a serpentine flow channel over a porous electrode. The non-dimensional average flow velocity in the flow channel decreases from the entrance to the fully developed flow region while an opposite trend is found in the porous layer. The

volumetric flow rate in the porous layer increases as the thickness of porous layer increases from 0.041 cm to 0.287 cm (the number of porous layers ranges from 1 to 7) for the carbon fiber paper electrodes.

Moreover, a model for describing the maximum current density is developed which estimates the stoichiometric availability of reactant in the porous layer for reaction. Under the inlet condition ($Q_{in} = 20 \text{ ml min}^{-1}$ or $u_{in} = 33.3 \text{ cm s}^{-1}$), the volumetric flow in the electrode layer, Q_p increases from $7.81 \times 10^{-4} \text{ cm}^3 \text{ s}^{-1}$ to $1.5 \times 10^{-3} \text{ cm}^3 \text{ s}^{-1}$ when the electrode thickness increases from one to three layers of carbon paper. Under these conditions, the maximum current density increases from 377 mA cm^{-2} to 724 mA cm^{-2} as the electrode thickness is increased. Predicted maximum current densities are compared with experimental results with agreement well within the uncertainty in the measurements of limiting current densities and estimated values of the permeability of the porous layers (377 mA cm^{-2} predicted vs. $\sim 400 \text{ mA cm}^{-2}$ measured for 1 layer, and 724 mA cm^{-2} predicted vs. $\sim 750 \text{ mA cm}^{-2}$ measured for 3 layers).

Acknowledgment

This work is partially supported by the “All Iron Flow Battery” project (DE-AR0000352) funded from Department of Energy (DOE) of the United States. We thank N.C. Hoyt for advice on the volumetric flow in the porous electrode. We appreciate the discussions with Dr. D.L. Feke and Dr. Paul Barnhart on the boundary conditions of our model. We gratefully acknowledge detailed information of materials and designs from Dr. A.Z. Weber from Lawrence Berkeley National Laboratory and Dr. M.M. Mench from the Department of Mechanical, Aerospace and Biomedical Engineering at University of Tennessee, Knoxville.

Nomenclature

a_s	active surface area (cm^{-1})
BC	boundary condition
c	concentration (mol cm^{-3})
d	diameter (μm)
D	diffusivity ($\text{cm}^2 \text{ s}^{-1}$)
F	Faraday constant ($96,485 \text{ C mol}^{-1}$)
\mathbf{g}	gravity acceleration vector (980 cm s^{-2})
g	gravity acceleration (980 cm s^{-2})
i	current density (mA cm^{-2})
k	permeability of the porous electrode (m^2)
$\mathbf{k}_{\gamma\sigma}$	permeability tensor for γ phase and σ phase of the porous electrode (m^2)
KC	Kozeny-Carman
L	length (cm)
P	pressure (Pa)
$\langle P \rangle$	average pressure (Pa)
$\langle P_{\gamma} \rangle$	intrinsic average pressure within γ phase (Pa)
Q	volumetric flow rate (ml min^{-1} or $\text{cm}^3 \text{ s}^{-1}$)
T	temperature (K)
t	thickness (cm)
X	X direction
Y	Y direction
Z	Z direction
\mathbf{u}	velocity vector (cm s^{-1})
u	X direction velocity (cm s^{-1})
$\langle u \rangle$	average X direction velocity (cm s^{-1})
V	volume of the representative porous element (μm^3)
v	Y direction velocity (cm s^{-1})
$\langle v \rangle$	average Y direction velocity (cm s^{-1})
w	width (cm)

Greek symbols

γ	liquid phase
ϵ	porosity
ι	characteristic length in a representative porous element (μm)
μ	dynamic viscosity (Pa s)
ρ	density of electrolyte fluid (kg m^{-3})
Σ	interface
σ	solid phase
Ω	domain

Subscripts

avg	average value
cf	between current collector and flow channel
e	entrance
eff	effective
f	flow domain
fi	fiber
fp	between flow channel and porous layer
in	inlet
lim	limiting
max	maximum
p	porous domain
pe	porous element
pm	between porous layer and ion selective membrane
po	pore

Dimensionless number

Re	Reynolds number ($\rho u_{in} t_f / \mu$)
----	---

References

- [1] M. Skyllas-Kazacos, C. Menictas, in: Proceedings of 19th International Telecommunications Energy Conference-INTELEC 1997, Melbourne, Australia, October 1997, pp. 19–23.
- [2] M. Skyllas-Kazacos, D. Kasherman, D. Hong, M. Kazacos, J. Power Sources 35 (1991) 399–404.
- [3] M. Skyllas-Kazacos, M. Rychcik, R.G. Robins, A.G. Fane, M.A. Green, J. Electrochem. Soc. 133 (1986) 1057–1058.
- [4] M. Skyllas-Kazacos, M. Rychcik, R.G. Robins, US Patent 4,786,567, USA, 1988.
- [5] Redox Flow Cell Development and Demonstration Project, NASA TM-97067, National Aeronautics and Space Administration, Washington, DC, 1979.
- [6] L.H. Thaller, Department of Energy, Washington, DC, DOE/NASA/1002-79/3, National Aeronautics and Space Administration, Washington, DC, NASA TM-79143, 1979.
- [7] R.J. Remick, P.G.P. Ang, USA Patent 4,485,154, 1984.
- [8] K.J. Cathro, K. Cedzynska, D.C. Constable, J. Power Sources 19 (1987) 337–356.
- [9] L.W. Hruska, R.F. Savinell, J. Electrochem. Soc. 128 (1981) 18–25.
- [10] M. Duduta, B. Ho, V.C. Wood, P. Limthongkul, V.E. Brunini, W.C. Carter, Y.-M. Chiang, Adv. Energy Mater. 1 (2011) 511–516.
- [11] B. Huskinson, M.P. Marshak, C.W. Suh, S. Er, M.R. Gerhardt, C.J. Galvin, X. Chen, A.A. Guzik, R.G. Gordon, M.J. Aziz, Nature 505 (2014) 195–198.
- [12] K.W. Knehr, E. Agar, C.R. Dennison, A.R. Kalidindi, E.C. Kumbur, J. Electrochem. Soc. 159 (2012) A1446–A1459.
- [13] A.A. Shah, R. Tangirala, R. Singh, R.G.A. Wills, F.C. Walsh, J. Electrochem. Soc. 158 (6) (2011) A671–A677.
- [14] A.A. Shah, M.J. Watt-Smith, F.C. Walsh, Electrochim. Acta 53 (2008) 8087–8100.
- [15] H. Al-Fetlawi, A.A. Shah, F.C. Walsh, Electrochim. Acta 55 (2009) 78–89.
- [16] A.A. Shah, H. Al-Fetlawi, F.C. Walsh, Electrochim. Acta 55 (2010) 1125–1139.
- [17] H. Al-Fetlawi, A.A. Shah, F.C. Walsh, Electrochim. Acta 55 (2010) 3192–3205.
- [18] M. Vynnycky, Energy 36 (2011) 2242–2256.
- [19] E. Kjeang, B.T. Proctor, A.G. Brolø, D.A. Harrington, N. Djilali, D. Sinton, Electrochim. Acta 52 (2007) 4942–4946.
- [20] D. Aaron, Z. Tang, A.B. Papandrew, T.A. Zawodzinski, J. Appl. Electrochem 41 (2011) 1175–1182.
- [21] D.S. Aaron, Q. Liu, Z. Tang, G.M. Grim, A.B. Papandrew, A. Turhan, T.A. Zawodzinski, M.M. Mench, J. Power Sources 206 (2012) 450–453.
- [22] Q. Liu, G.M. Grim, A.B. Papandrew, A. Turhan, T.A. Zawodzinski, M.M. Mench, J. Electrochem. Soc. 159 (2012) A1246–A1252.
- [23] J. Chen, B. Wang, H. Lv, Adv. Mater. Res. 236–238 (2011) 604–607.
- [24] Q. Xu, T. Zhao, P. Leung, Appl. Energy 105 (2013) 47–56.
- [25] T.J. Latha, S. Jayanti, J. Power Sources 248 (2014) 140–146.
- [26] Z. Yang, J. Zhang, M.C.W. Kintner-Meyer, X. Lu, D. Choi, J.P. Lemmon, J. Liu, Chem. Rev. 111 (2011) 3577–3613.
- [27] M. Skyllas-Kazacos, M.H. Chakrabarti, S.A. Hajimolana, F.S. Mjalli, M. Saleem, J. Electrochem. Soc. 158 (2011) R55–R79.
- [28] A.Z. Weber, M.M. Mench, J.P. Meyers, P.N. Ross, J.T. Gostick, Q. Liu, J. Appl. Electrochem. 41 (2011) 1137–1164.
- [29] P. Leung, X. Li, Carlos Ponce de León, L. Berlouis, C.T. John Low, F.C. Walsh, RSC Adv. 27 (2012) 10125–10156.
- [30] S. Whitaker, Chem. Eng. Sci. 28 (1973) 139–147.
- [31] S. Whitaker, AIChE J. 13 (1967) 420–427.
- [32] S. Whitaker, Transp. Porous Media 1 (1986) 3–25.
- [33] S. Whitaker, The Method of Volume Averaging, Kluwer Academic Publishers, Norwell, 1999.
- [34] W.G. Gary, K. O'Neill, Water Resour. Res. 12 (1976) 148–154.
- [35] F.A. Howes, S. Whitaker, Chem. Eng. Sci. 40 (1985) 1387–1392.
- [36] J.A. Ochoa-Tapia, S. Whitaker, Int. J. Heat Mass Transfer 38 (1995) 2635–2646.
- [37] J.A. Ochoa-Tapia, S. Whitaker, Int. J. Heat Mass Transfer 38 (1995) 2647–2655.
- [38] B. Goyeau, D. Lhuillier, D. Gobin, M.G. Velarde, Int. J. Heat Mass Transfer 46 (2003) 4071–4081.
- [39] M.L. Bars, M.G. Worster, J. Fluid Mech. 550 (2006) 149–173.
- [40] H.C. Brinkman, Appl. Sci. Res. A1 (1947) 27–34.
- [41] G.S. Beavers, D.D. Joseph, J. Fluid Mech. 30 (1) (1967) 197–207.
- [42] P.G. Saffman, Stud. Appl. Math. 1 (1971) 93–101.
- [43] G. Neale, W. Nader, Can. J. Chem. Eng. 52 (1974) 475–478.
- [44] W.O. Williams, Quart. Appl. Math. 36 (1978) 255–268.
- [45] K. Vafai, S.J. Kim, Int. J. Heat Fluid Flow. 11 (1990) 254–256.
- [46] K. Vafai, R. Thiyagaraja, Int. J. Heat Mass Transfer 30 (1987) 1391–1405.
- [47] B. Alazmi, K. Vafai, Int. J. Heat Mass Transfer 44 (2001) 1735–1749.
- [48] S.J. Kim, C.Y. Choi, Int. J. Heat Mass Transfer 39 (1996) 319–329.
- [49] D. Poulikakos, M. Kazmierczak, J. Heat Transfer 109 (1987) 653–662.
- [50] M. Chandesris, D. Jamet, Int. J. Heat Mass Transfer 49 (2006) 2137–2150.
- [51] M. Chandesris, D. Jamet, Int. J. Heat Mass Transfer 50 (2007) 3422–3436.
- [52] M. Ehrhardt, An Introduction to Fluid-porous Interface Coupling, <http://www.math.uni-wuppertal.de>, (accessed May 2014).
- [53] V. Laptev, Numerical Solution of Coupled Flow in Plain and Porous Media (Ph.D. thesis), University of Kaiserslautern, 2003.
- [54] A. Tang, J. Bao, M. Skyllas-Kazacos, J. Power Sources 248 (2014) 154–162.
- [55] G. Qiu, C.R. Dennison, K.W. Knehr, E.C. Kumbur, Y. Sun, J. Power Sources 219 (2012) 223–234.
- [56] J. Kozeny, Stizungsber Akad. Wiss. Wien. 136 (1927) 271–306.
- [57] P.C. Carman, Trans. Inst. Chem. Eng. Lond. 15 (1937) 150–166.
- [58] M.M. Tomadakis, T.J. Robertson, J. Compos. Mater. 39 (2005) 163–188.
- [59] R. Carta, S. Palmas, A.M. Polcaro, G. Tola, J. Appl. Electrochem 21 (1991) 793–798.
- [60] B. Atkinson, M.P. Brocklebank, C.C.H. Card, J.M. Smith, AIChE J. 15 (1969) 548–553.
- [61] R. Chen, J. Fluids Eng. 95 (1973) 153–158.
- [62] X. Ke, CFD Studies on Mass Transport in Redox Flow Batteries (M.Sc. thesis), Case Western Reserve University, 2014.
- [63] J.S. Newman, Electrochemical Systems, Prentice-Hall, Inc., Englewood Cliffs, 1973.